Estimating Water Content and Grain Size of Intertidal Flat Sediments Using Visible to Shortwave-Infrared Reflectance and Sentinel 2A Data: A Case Study of the Red River Delta, Vietnam

Vu Thi Thu Thuy [ID], Nguyen Thi Thu Ha [ID], Katsuaki Koike [ID], Nguyen Thien Phuong Thao [ID], Pham Ngoc Trung, and Dinh Xuan Thanh

Abstract—Sediment properties such as water content (WC) and grain size (GS) are essential to characterize the environmental conditions of tidal flats. This article aimed to develop appropriate models to estimate the WC and GS of surface sediments for an intertidal flat on the Red river delta (Vietnam) using Sentinel 2A (S2A) images. The spectral reflectance, WC, and GS of 96 subsamples from 12 sediment samples collected on December 17, 2017 were measured to clarify their relationships. The WC was highly correlated with the reflectance ratio of two shortwave-infrared bands, $R(2190)/R(1610)$ ($R^2 = 0.93$). The median GS (D_{50}) at 0%, 15%, and 20% of WC was significantly correlated with the reflectance ratio of the near-infrared band (842 nm) versus the visible-green band (560 nm) ($R^2 > 0.78$). Next, D_{50} was estimated from a multivariate regression model using this band ratio, the visible-red band (665 nm), and WC. The accuracy of the models was verified by comparisons with WC and D_{50} from 20 samples collected on March 12th 2019 (RMSE of both WC and D_{50} < 15%). Then, the WC and sediment type distributions were mapped by applying these models to two S2A scenes. The maps showed high WC (>30%) in very fine sediments (silts), which is consistent with other intertidal flats with similar sediment types. This article was limited to fine sediment samples. Therefore, our next step is to incorporate coarse sediments into the models to provide more universal mapping of WC and sediment types.

Index Terms—Hyperspectral imaging, land surface, remote sensing, sediments, soil properties.

Vu Thi Thu Thuy is with the Graduate School of Engineering, Kyoto University, Kyoto 615-8540, Japan, and also with the Department of Geography, Hanoi National University of Education, Hanoi 10000, Vietnam (e-mail: vu.thuy.63x@st.kyoto-u.ac.jp).

Nguyen Thi Thu Ha, Nguyen Thien Phuong Thao, Pham Ngoc Trung, and Dinh Xuan Thanh are with the Faculty of Geology, University of Science, Vietnam National University, Hanoi 10000, Vietnam (e-mail: hantt_kdc@vnu.edu.vn; nguyenthienphuongthao_t57@hus.edu.vn; phamngoctrung_t60@hus.edu.vn; dxthanh@vnu.edu.vn).

Katsuaki Koike is with the Graduate School of Engineering, Kyoto University, Kyoto 615-8540, Japan (e-mail: koike.katsuaki.5x@kyoto-u.ac.jp).

I. INTRODUCTION

INTERTIDAL flats composed of muddy sediments form an important part of marine ecosystems. Changes in the sediment properties of intertidal flats, such as the water content (WC), grain size (GS), type, mineral and chemical compositions, and organic matter content (OM) of sediments, and their spatio-temporal distributions affect the intertidal environment and, accordingly, the life of marine organisms, particularly benthic communities [1], [2]. The WC and GS are among the most important features of the intertidal environment because they control sedimentary processes and diagenesis including transport, precipitation, compaction, and erosion [3]. The WC is determined by the duration of inundation and exposure of the intertidal flats, air temperature, and marsh plant density [4]. The GS distribution generally varies from the land towards the sea depending on the heterogeneous conditions of transport, accumulation, and hydrodynamics related to tidal and wave energies in estuaries [5]. Importantly, GS affects vulnerability to heavy metal pollution [6] and biogeochemical remediation of polluted sediments. A typical pattern of pollution is that the level increases with decreasing particle size, i.e., contaminants accumulate more easily in fine sediments [7]–[9]. Therefore, accurate estimations of the WC and GS of sediments are essential to clarify the conditions of intertidal environments, their spatio-temporal change, and the factors influencing that change.

Remote sensing has been used since the 1980s for estimating WC through the reflectance absorption caused by the O–H vibration of water molecules [10], as well as for estimating GS and mapping sediment type (such as silty or sandy soil) over intertidal flats based on the typical GS range [11]. Remote sensing has also been used to estimate OM [12], [13]. Mapping sediment types has been conducted using spectral features in the visible (VIS), and near- and shortwave-infrared (NIR and SWIR) regions acquired by various multispectral [11], [14] and synthetic aperture radar [15] sensors on satellites, hyperspectral aircraft [16], and unmanned aerial vehicles [17]. Typical multispectral optical sensors for sediment-type mapping include Terra/ASTER, ALOS, Sentinel 2, Landsat, and SPOT; the TM, ETM+, and OLI sensor images of the Landsat series have been applied the most [11], [14], [15], [18], [19]. Conventional

mapping methods construct regression models between selected spectral features and statistical parameters of GS (e.g., the median GS, D_{50}). Although regression models are simple, their effectiveness has been demonstrated by many case studies [15], [16], [18].

Previous studies have shown that particle size estimations from surface reflectance within VIS-SWIR regions are influenced by many factors, such as WC [19], OM [20], mineral composition [21], [22], porosity [23] of sediment samples, or viewing angle in reflectance measuring techniques [24]. Few studies, however, have considered these influences when selecting suitable bands or band combinations to develop models for particle size estimation, particularly in preceding satellite-based regression models. Consequently, these models are sometimes applied with insufficient understanding of their limitations or poor performance.

The spatial and spectral resolutions of the multispectral instrument (MSI) imagery of Sentinel 2A (S2A), launched in June 2015 as a part of the European Space Agency's Copernicus Program, are higher than those of the Landsat series. Therefore, more accurate mapping of sediment types may be possible with S2A MSI imagery. Although the effectiveness of S2A MSI imagery has been shown for geological applications, such as lithological and facies mapping in an arid to semiarid region [25], tracing iron-bearing minerals in a mining district [26], mapping hydrothermal alteration minerals [27], and delineating granite blocks in a weathered and vegetated coastal zone [28], its application to intertidal flats to date is limited to a study by [29] because of the short operational period since its launch. Marchetti *et al.* [30] investigated the potential of S2A to classify fine to coarse sediment types on river bars based on imagery from a near ground unmanned aerial vehicle and demonstrated a high correlation between SWIR reflectance and D_{50}. However, the effect of the sediment WC was not considered in estimating the GS in that study, and it is known that the SWIR reflectance will change with WC. No methods have been proposed for estimating both the WC and GS of intertidal sediments using S2A reflectance data. This limitation does not allow the full potential of the S2A data to be extracted.

Therefore, this article aimed to develop methods that can accurately estimate sediment WC and D_{50} from S2A imagery using VIS, NIR, and SWIR reflectance and *in situ* WC and D_{50} data from intertidal sediments. An intertidal flat in the Red river delta, Vietnam, was selected as a case study for mapping sediment type, monitoring its environmental change, and identifying the factors influencing that change.

II. Materials and Methods

A. Study Area

The study area is situated on the southeast coast of the Red river delta and is the left side of the fan-shaped estuary of the day river [see Fig. 1(a)]. The intertidal flat is formed by the interaction of the day river and the coastal area, with diurnal and meso-tidal tide cycles ranging from 0.1 to 3.7 m (mean, 2.3 m) [31]. During the high-tide period in spring, the study area is submerged to a depth of 2 m. The total area of approximately
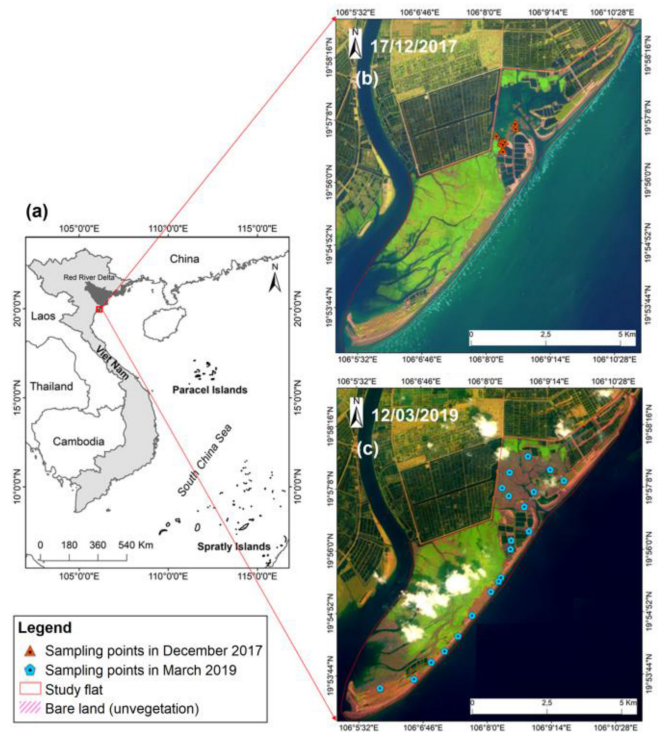

Fig. 1. (a) Location of the studied tidal flat on the Red river delta, Vietnam. (b) Location of 12 sampling sites in the initial field campaign on December 17, 2017 overlaid on a false color composite (R: band 11, G: band 8, B: band 2) S2A image acquired on the same date. (c) Location of 20 sampling sites in the subsequent field campaign on March 12, 2019 overlaid on a similar false color composite S2A image acquired on March 12, 2019.

$27 \, \text{km}^2$ is composed of mangrove forest ($9.5 \, \text{km}^2$), shrimp ponds ($5 \, \text{km}^2$), and unvegetated flat ($12.5 \, \text{km}^2$). The Hai Phong Institute of Oceanography (renamed Institute of Marine Environment and Resources) reported in 2003 that the intertidal flat was covered by four main sediment types: grey; micaceous; and fine-grain sand (D_{50}: 102–131 μm) from the mean low water line to the mean sea level (MSL); greyish brown coarse silt (D_{50}: 58–95 μm) between the 2 m water depth to MSL; reddish brown silty mud (D_{50}: 15–47 μm) between MSL and the mean high water line (MHWL); and reddish brown clayey mud (D_{50}: 9–10 μm) in the Day river bed and the top soil of the mangrove forest between MHWL and the mean higher high water line [32]. The main source of the sediments is weathered metamorphic rock in the upper part of the Red river basin; tectonic activities along the Red river fault system have fractured the rocks and advanced the weathering [33].

B. Field Sampling and Measurement

Sediment samples of approximately 500 g were taken from the ground surface up to 3 cm depth on exposed areas of the flat on December 17, 2017 (initial 12 samples) and March 12, 2019 (subsequent 20 samples). The sample sites included a wide range of GS and various geographical features such as upper tidal and intertidal zones, sand bars, and the water line. They were precisely positioned using a GPS Etrex 10 (Garmin, Kansas, U.S.).

According to the tide tables in 2017 and 2019 [31], the tide level at the local time of the S2A image acquisition over the study flat at about 10:00 to 11:00 am (3:00 to 4:00 am GMT) on December 17th 2017 ranged from 1.5 to 1.8 m, whereas on March 12, 2019 it ranged from 0.6 to 0.8 m. Therefore, the intertidal flat was mostly submerged on the former date [see Fig. 1(b)], and completely exposed on the latter date [see Fig. 1(c)]. Owing to the effect of tide level, the locations of the initial 12 samples and subsequent 20 samples on the flat were distributed closely and more widely, respectively (see Fig. 1).

Field reflectance was measured in the initial sampling period in the nadir direction with approximately 10° view zenith angle, similar to the view zenith angle of the S2A sensor [34] and at 20 cm above the flat surface using the standard pistol grip of a portable FieldSpec3 Max spectroradiometer (ASD Inc., Boulder, U.S.). The measurements were taken within 30 minutes of the S2A image acquisition time. The FieldSpec3 Max measures reflectance and fluxes at wavelengths of 350–2500 nm with 3–10 nm fullwidth half-maximum splined to a spectral output of 1 nm [35]. The field reflectance was transformed to the S2A band reflectance using the spectral response function from Brasi *et al.* [36]. The transformed field reflectance allowed the effect of atmosphere to be corrected during the image preprocessing stage. Among the 12 measured points of the initial sampling period, the data at two points were lower quality with substantial noise levels and these were discarded in subsequent analysis.

Each sediment sample was collected using a stainless-steel spade, placed in a plastic zipper bag and then stored in an icebox prior to the measurement of WC, GS, and OM using standard methods in a laboratory.

C. Laboratory Analysis Methods

The GS of sediment is defined as the mean size of the grains in a sediment sample [37], which can be expressed by percentages of component grains [38] or by the median particle diameter, D_{50}, of the sample [39]. In the laboratory, sediment samples were first air-dried and then lightly crushed using a sterile agate mortar prior to sieving following the ASTM D6913 [40] to determine the percentage of grains with a particle diameter larger than 75 μm. The GS of samples smaller than a No. 200 (75 μm) sieve were analyzed using a laser diffraction particle size analyzer (LA-950 Laser Particle Size Analyzer, Horiba, Japan) with the guidance of the D7928 [41]. The D_{50} was specified from the cumulative GS distribution using a statistical package [42], where D_{50} is the particle size at 50% of the cumulative percentage. The D_{50} of all the samples ranged from 5 to 163 μm. Next, the WC was determined by the mass loss of the wet sample after drying at 110 °C in an oven for 16 h and the OM was determined by the dried sample being heated gradually to 750 °C in a furnace (SMF-2, AS ONE, Japan) and being kept at this temperature for at least one hour, until no change in the mass occurred, respectively, according to the ASTM D2974 [43]. The OM value determined by this method may be slightly larger than the actual value because the mass lost during heating at temperatures higher than 400 °C includes the mass of mineral structural water [44].

To investigate the effect of WC on the reflectance spectra of a sample, the initial 12 samples collected on December 17, 2017 were saturated with sea water and then each sample was divided into eight sub-samples (total of 96 sub-samples). The sub-samples were dried in an oven for eight different time spans (0 to 60 min at 10-min intervals, and 6 h) to provide eight different WC conditions.

The reflectance spectra of the 96 subsamples with different WC conditions were measured in the laboratory with the same direction and angle as the field reflectance measurement using the standard contact probe of the FieldSpec3 mentioned above. The probe was installed constantly in the nadir direction so that the sapphire window touched the sample's surface in a dark box environment according to the protocol in [45]. The data were also transformed to S2A band reflectance using the spectral response function [46] to analyze their correlations with the WC and D_{50} to identify the most suitable S2A bands or band combinations to estimate these two parameters. The best models were verified by estimating WC and D_{50} from the S2A image acquired on March 12, 2019 using the models and comparing the results with *in situ* WC and D_{50} data from the subsequent 20 samples collected on that date.

D. Image Processing and Mapping Methods

Two S2A level 1C scenes acquired at 10:16 am (local time) on December 17, 2017 (ID: S2A_MSIL1C_ 20171217T032131_N0206_R118_T48QXH) and March 12, 2019 (ID: S2A_MSIL1C_20190312T031541_ N0207_R118 _T48QXH) were downloaded from the Copernicus open access hub. The S2A level 1C images are geometrically corrected and georeferenced to the UTM/WGS84 projection before release. To estimate surface WC and other physical properties, the atmospheric effects on optical sensor image data must be removed [47]. The empirical linear model (ELM) method [48] is the most accurate atmospheric correction method for S2A image data [49], [50]. Therefore, per-pixel reflectance at the top of atmosphere (TOA) of the images was transformed into the bottom of atmosphere (BOA) reflectance through ELM to allow a linear regression between the mean field reflectance at the ten field sample points and the TOA reflectance of the ten corresponding pixels of the S2A image.

Finally, the BOA reflectance of the S2A image on March 12, 2019 was used to map the WC and D_{50} distributions over the study area from the regression models. First, the unvegetated intertidal flat zone was delineated from the image. Then the best models were used to estimate WC and D_{50} in all pixels of the zone. The estimated D_{50} was classified using the thresholds of the Wentworth scale [39] to map the sediment types over the intertidal flat. The flowchart of these procedures and the study methodology are shown in Fig. 2.

III. RESULTS

A. Characterization of Sediment Types Over the Study Area

Table I gives the GS, WC, and OM features of the 32 sediment samples used in this article. The twelve samples collected on
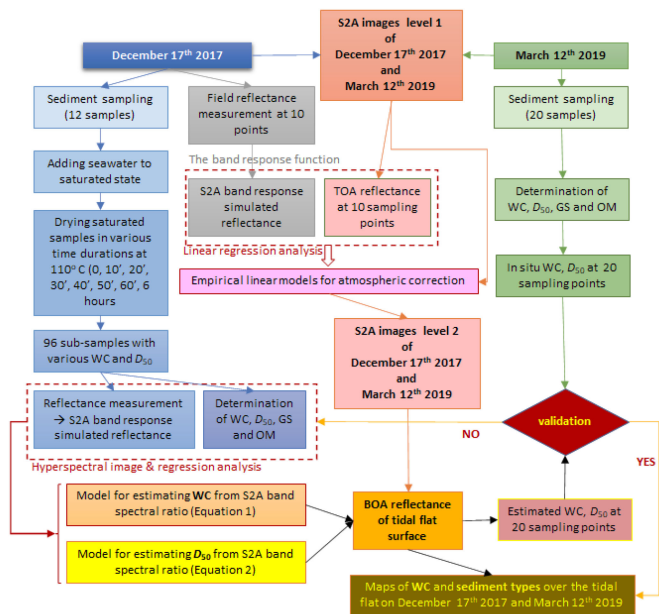
Fig. 2. Methodology flowchart for the mapping WC and median GS from sediment samples and S2A images over the study area.
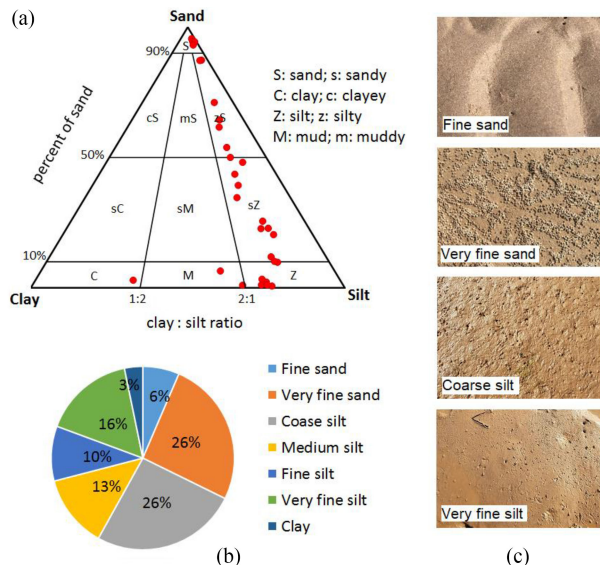

Fig. 3. Classifications of 32 sediment samples from the study area in the Red river delta (see Fig. 1) by (a) GS ternary diagram following the Folk classification criterion [38]. (b) Sediment types based on D_{50} and the Wentworth scale [39]. The photographs in (c) show the typical appearance of the four common sediment types in the study area.

TABLE I
FEATURES OF SEDIMENT SAMPLES USED FOR MODEL DEVELOPMENT AND VALIDATION

Dataset	Date of sampling	No. of sample/ subsample	WC (%) *	D_{50} (µm)*	OM (%) *
Model development	Dec. 17th 2017	12/96	0.00/ 40.36/ 15.79	5.0/ 163.0/ 65.0	1.06/ 12.70/ 3.63
Model validation	Mar. 12th 2019	20/0	3.40/ 39.00/ 26.30	28.6/ 95.0/ 69.2	2.90/ 7.98/ 4.00

*Minimum/Maximum/ Mean.

December 17, 2017 were divided into 96 subsamples. The WC data for the model development were obtained by adding eight different levels of water to the dry sediment samples. In contrast, the WC data for the model verification was the natural WC of samples collected on the immediate intertidal surface at the acquisition time of the S2A image on March 12, 2019.

Following the Folk classification criterion [38], the 32 samples were classified into six sediment types based on the GS distribution: sand, silty sand, sandy silt, silt, clayey silt (mud), and clay. The samples were characterized mainly as silty sediments, because the silt-related types (sandy silt, silt, and clayey silt) made up 61% of the total samples [see Fig. 3(a)]. The overall OM was low and ranged from 1.06% to 12.7% with a mean of 3.63%, which supports the negligible effect of OM on the determination of D_{50} of fine sediments [51]. Following the Wentworth scale for D_{50}, the sediment samples were divided into five types

[see Fig. 3(b)] in which the D_{50} of very fine sand (63–125 µm) and coarse silt (31–63 µm) made up the first and second largest proportions of the samples, 63% and 26%, respectively. There were only small variations in the GS distribution indicating that most samples were well sorted. The sediment types and GS characteristics of the samples reflected the common sediments of large river systems under tide-dominated deltaic settings [52], such as the Amazon River [53] and Changjiang River [54], and they were similar to the surface sediments of other tidal flats from the Red river mouth to the day river estuary [55], [56].

The 12 initial samples showed the D_{50} ranged from 5 to 163 µm. The samples were classified into four types: very fine silt ($N = 3$, D_{50}: 3.9–7.8 µm); coarse silt ($N = 3$, D_{50}: 31–63 µm); very fine sand ($N = 5$, D_{50}: 63–125 µm); and fine sand ($N = 1$, D_{50}: 125–250 µm). The colors of the sample types were similar, i.e., the fine sand and very fine sand samples were grey, the coarse silt samples were greyish brown, and the very fine silt samples were reddish brown [see Fig. 3(c)]. Owing to these two features, the reflectance spectra of the 12 samples under almost the same measurement conditions, such as illumination, distance between the sensor and sample, view direction, and incident zenith angle, expressed typical spectral patterns for each sediment type with similar WC.

Like the common sediment-type distribution in tidal flats described in [57], the sediments in the study area became finer towards the land, i.e., the coarse sediments were distributed in the lower sections of the tidal flat, whereas the higher sections were covered with very fine sediments. Fine sands formed a sand flat with wave ripples near and/or below the water line [the top photograph in Fig. 3(c)] and at the bottom of tidal creeks and the sub-tidal zone below the low tide mark. The intertidal zone [see Fig. 1(c)] between the high and low tide marks and the unvegetated zone was mostly covered by a typical
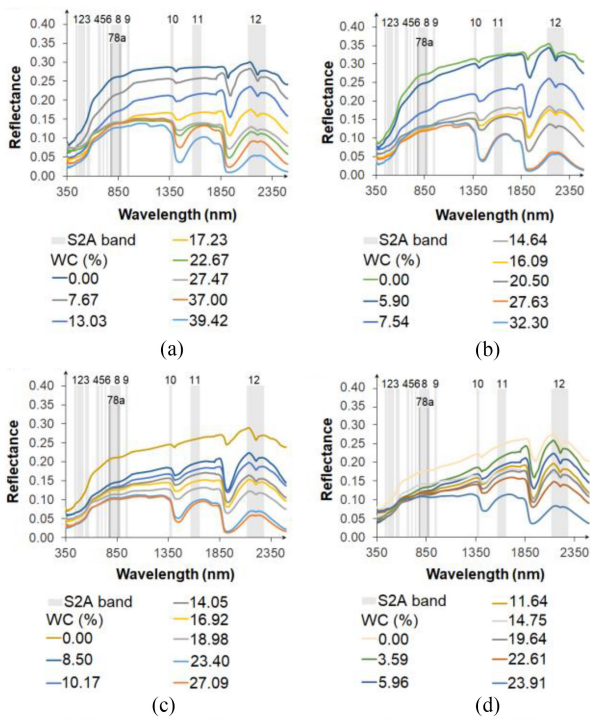
Fig. 4.   Changes in the reflectance spectra of four representative sediment types based on D_{50} and the Wentworth scale [39]. (a) Very fine silt. (b) Coarse silt. (c) Very fine sand. (d) Fine sand, with the different WCs. The wavelengths of the S2A twelve bands underlie the spectra.

Fig. 5.   Correlation between WC and (a) the simulated reflectance at S2A band 12, (b) R(B12) excluding WC = 0 % data, (c) reflectance ratio of B12 versus band 11, R(B12)/R(B11), and (d) R(B12)/R(B11) excluding WC = 0 % data. The best regression curves of negative logarithmic [(a) and (b)] or linear [(c) and (d)] functions are overlaid on each graph. R^2 and RMSE denote the coefficient of determination and root-mean-squares error, respectively.

fine silt sediment. Another fine type, the clay sediments, was distributed on the highest flat, the supratidal zone covered by mangroves. The present samples corresponded to the sediment characteristics in the studied flat reported by [32].

B. Effect of WC on the Reflectance Spectra

The porosity of intertidal flat sediment tends to increase with decreasing GS and, therefore, the WC tends to be greater in fine sediments. The resultant WCs in a saturated state followed this general trend, i.e., very fine silt: 38.73%–40.36%, coarse silt: 25.01%–32.23%, very fine sand: 23.22%–27.09%, and fine sand: 23.24%. The effect of the WC clearly appeared in the high reflectance absorption of the fine-grain sediment (very fine silt) which demonstrated more prominent water absorption bands compared with the spectra of wet coarser-grain sediment (fine sand) as shown in Fig. 4(a) and (d). Only band 12 (B12) contained a water absorption band at 2200 nm (see Fig. 4), confirming its importance for estimating WC from the S2A image.

In all the representative samples of the four sediment types based on D_{50} (fine sand, very fine sand, coarse silt, and very fine silt), the reflectance, $R(\lambda)$ (λ means wavelength) changed substantially with WC and decreased systematically with increasing WC (see Fig. 4). In particular, the $R(\lambda)$ in the SWIR region longer than 1400 nm decreased more than those in VIS (400–700 nm) and NIR (700–900 nm) regions. The decrease in $R(\lambda)$ became larger with longer wavelengths. The largest decrease occurred in the longest S2A band, SWIR B12 (centered on 2190 nm), with
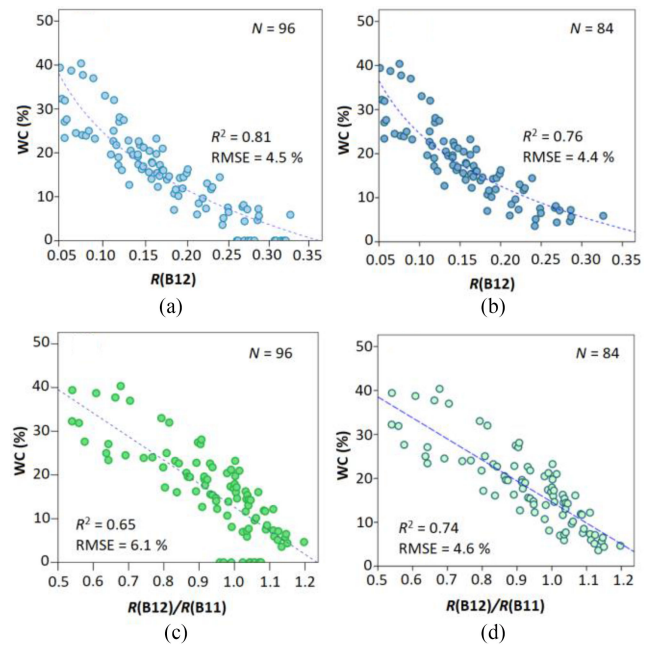
a slightly smaller decrease in the shorter SWIR B11 (centered on 1610 nm). A feature of B12 was that the $R(\lambda)$ decline within the absorption bands became less conspicuous with increasing WC and disappeared completely at the highest WC level at 23.91%–39.42%. The difference in $R(\lambda)$ between B11 and B12 depending on WC was used to discriminate WC in the S2A image data.

A substantial decrease in $R(\lambda)$ with increasing WC was also observed in B9, centered on 945 nm, and B10, centered on 1375 nm. However, because these two bands are sensitive to the water vapor in the atmosphere [58], they could not be used in S2A-based WC estimation.

The correlation of each simulated S2A band reflectance, R(B[band number]), with WC was examined first. The Pearson correlation coefficients (ρ) for the simulated reflectance at SWIR B10, B11, and B12 for the 96 sub-samples collected on December 17. 2017 with WC were: -0.83 (B10); -0.88 (B11); and -0.91 (B12), respectively, whereas the ρ values of remaining single bands were much smaller, ranging between 0.61 and 0.67. All available S2A band ratios were considered for WC and only those ratios with $\rho > 0.7$ were selected. Two ratios—R(B12)/R(B11) and R(B12)/R(B8)—satisfied this condition with the highest and second highest correlations with WC of $\rho = -0.81$ and -0.72, respectively. Close correlations between these band parameters and WC were confirmed by their scatter-plots (see Fig. 5). Consequently, R(B12) and R(B12)/R(B11) were identified as the most suitable band and band ratio for S2A band-based WC estimation.
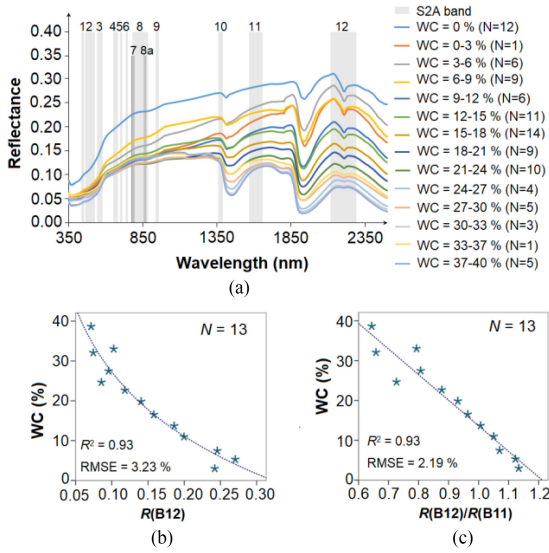
Fig. 6. (a) Changes in reflectance spectra for 14 groups of sediment sub-samples, overlaid with the S2A band locations. (b) Relationship between WC and R(B12). (c) Relationship between WC and R(B12)/R(B11) for the groups with WC > 0 %. The regression curves in (b) and (c) are the best fit with the maximum R^2.

Fig. 7. Reflectance spectra of the initial 12 samples with different D_{50} under three WC conditions with S2A bands. (a) Fully dry (WC = 0 %). (b) Half-saturated (almost half the WC of full saturation). (c) Fully saturated.

WC = 0% meant a completely dry condition. This condition is seldom satisfied on the surface of an intertidal flat. Therefore, the regression curves excluded the WC = 0% data as shown in Fig. 5(b) and (d). The best fit regressions were obtained by a logarithmic relationship for R(B12) [see Fig. 5(b)], and a linear relationship for R(B12)/R(B11) [see Fig. 5(d)]. Their fit was confirmed by a high R^2 (0.81 and 0.74, respectively).

To clarify the relationship between WC and R(B12) and R(B12)/R(B11) more in detail, the reflectance spectra of all 96 sub-samples were classified into 14 groups according to the 14 WC levels with a 3% interval, and the spectral data in each group were averaged [see Fig. 6(a)]. This process is termed group normalization. The most notable feature of the averaged 14 spectra was a decrease in R(λ)s with increasing WC. By excluding the spectral data of the group with WC = 0% as mentioned above, the R(B12) and R(B12)/R(B11) of the remaining 13 groups were correlated with WC [see Fig. 6(b) and (c), respectively]. The regression functions of each parameter were selected by the maximum R^2. Although the R^2 was the same for both the regression models, the RMSE of the band ratio model using the simplest, linear function was slightly smaller [see Fig. 6(c), N = 13]. Therefore, this regression model was specified as the best model for estimating WC for the study area, as follows:

$$\text{WC} = 77.89 - 64.27 * R\,(\text{B12})/R(\text{B11}). \quad (1)$$

C. Relationship Between Reflectance Spectra and Sediment Type

The relationship between the reflectance spectra of the initial 12 samples collected on December 17, 2017 and D_{50} was examined using the WC level (see Fig. 7). In addition to soil particles, many other components are contained in tidal flat sediments,
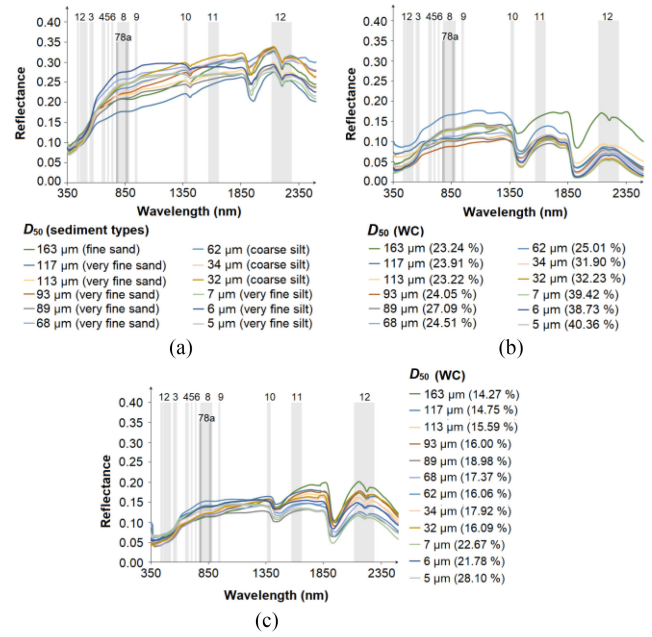
including water, OM, silicate minerals, and metal ions such as Fe^{2+}, Fe^{3+}, and Cu^{2+} [59], [60]. Therefore, the reflectance spectra from the initial 12 samples under dry conditions (WC = 0%) represented a combination of the reflectance spectra from all the components [see Fig. 7(a)]. Although the magnitude of reflectance was different with each sample, a general trend was common to all the samples, despite the variation in their D_{50}, in that R(λ) increased substantially from 400 to 1000 nm and remained almost constant within the range 1000 to 2500 nm. Other common spectral features and their causes were interpreted as follows. The small peak within 600–800 nm originated from the OM [20], [61] and the three small absorption peaks at 1400, 1900, and 2200 nm in SWIR were caused by vibration and bending of hydroxyl and water molecules contained mainly in silicate minerals [19], [62], [63]. The overall R(λ) magnitude, particularly R(B11) and R(B12), has been shown to increase with decreasing D_{50} [19]. However, this feature did not apply to the fully dried samples, as shown in Fig. 7(a), where the R(B11) and R(B12) of silts were smaller than those of the coarser sediments (sands). In this article, the small difference in D_{50} among sediment samples may be one explanation for the small difference in the scattering intensity from the surface particles. Therefore, the SWIR R(λ) data were not suitable for estimating D_{50}.

Like the correlation analysis with WC shown above, the sub-samples were classified into six groups by their D_{50} within a 6 μm range and then group normalization of the spectral data was applied for the three WC levels (0%, 15±2%, and 20±2%) in each group (see Fig. 8). No consistent relationship was found between R(B11), R(B12) and D_{50} that was common to the three WC levels. Figs. 4, 6, and 7(a) demonstrate that WC affected the overall magnitude of R(λ), but the effect of D_{50} was absent,
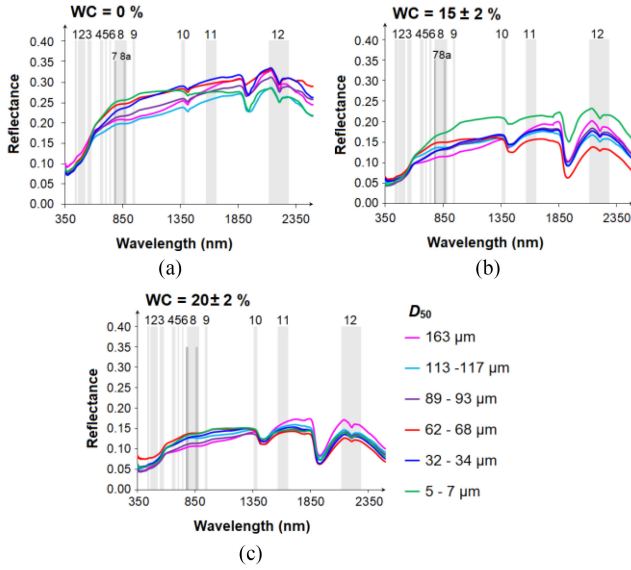
Fig. 8. Averaged reflectance spectra for six sediment groups for D_{50} at three WC levels with different S2A bands. (a) WC = 0 %. (b) WC = 15±2 %. (c) WC = 20±2 %. The D_{50} range in each group is within 6 μm.
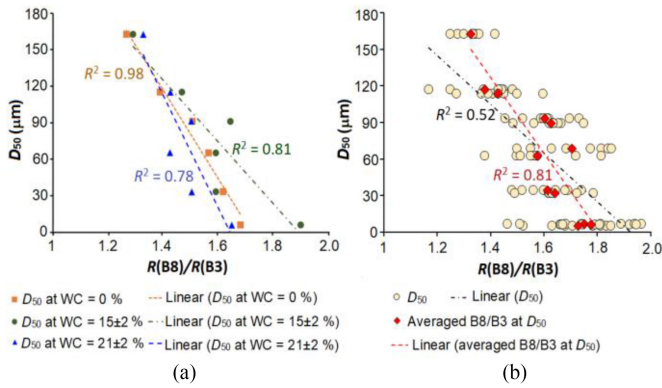

Fig. 9. Correlation between the D_{50} and the simulated S2A band ratio, B8 versus B3, $R(B8)/R(B3)$ of (a) six sediment groups at three WC levels, 0 %, 15±2 %, and 20±2 % colored orange, green, and blue, respectively, and (b) 96 subsamples without consideration of WC (black) with regression lines. The red marks in (b) denote the group normalization of B8/B3 based on D_{50}.

particularly in the SWIR region. Therefore, the correlation of R(λ) with D_{50} was examined in the VIS–NIR bands (B1–B8a). The highest correlations of D_{50} that were common to the three WC levels were observed with B8 and B8a ($\rho \geq 0.80$), which suggests these bands are important for estimating D_{50}.

The most noteworthy feature in Fig. 8 is that the $R(\lambda)$ increased linearly between B3 (543–578 nm) and B8, but the gradients differed with D_{50}, common to the WC levels. Therefore, the simulated S2A band ratio of B8 versus B3, $R(B8)/R(B3)$ was selected to analyze the correlation of D_{50}, in which the D_{50} data were averaged in each group, e.g., $D_{50} = 6$ μm was used for the $D_{50} = 5$–7 μm group in Fig. 8. Close negative relationships between the two parameters were common to the three WC levels with $\rho \geq 0.88$ ($R^2 \geq 0.78$) as shown in Fig. 9(a). The D_{50} and $R(B8)/R(B3)$ data of the 96 subsamples were plotted regardless of WC [see Fig. 9(b)] and a negative correlation was shown ($\rho = -0.72$, $R^2 = 0.52$). If the WC effect on B8/B3 was assumed to be

TABLE II
SUMMARY OF MULTIVARIATE REGRESSION MODELS FOR ESTIMATING D_{50} FROM SELECTED EXPLORATORY VARIABLES, $R(B8)/R(B3)$, WC, AND $R(B4)$

Model	Variable	R^2	Adjusted R^2	RMSE (μm)	F	p
NIR_Gr	$R(B8)/R(B3)$	0.52	0.51	34.1	101.54	0.00
R_W	$R(B8)/R(B3)$, WC	0.54	0.53	33.5	54.61	0.00
G_RNN	$R(B8)/R(B3)$, $R(B4)$	0.56	0.55	32.7	59.83	0.00
VNIR_W	$R(B8)/R(B3)$, WC, $R(B4)$	0.71	0.70	27.0	73.31	0.00

F and p denote the F-ratio and statistical significance of each coefficient, respectively.

negligible, the correlation of the group normalized B8/B3 with D_{50} became stronger [shown as red dots in Fig. 9(b)] with $\rho = -0.90$ and $R^2 = 0.81$. This suggests that D_{50} can be estimated directly from $R(B8)/R(B3)$ for sediments with a similar WC. Additionally, the importance of spatio-temporal changes in WC for the estimation of D_{50} was confirmed and was incorporated as a variable into the estimation model.

The color of the intertidal flat varied with the sediment type as described above. The most distinct color was red for fine sediments. Therefore, it was possible that the S2A red band, B4 (650–658 nm), could be used to estimate D_{50} together with $R(B8)/R(B3)$. To obtain a more accurate D_{50} estimation and construct the best regression model, $R(B8)/R(B3)$, WC, and $R(B4)$ were considered as explanatory variables in a multivariate analysis of the 96 subsamples. This multivariate analysis provided multivariate linear regression models of the D_{50} prediction from a set of explanatory variables, $R(B8)/R(B3)$, WC, and $R(B4)$. The best model was obtained with this combination, with a maximum adjusted $R^2 = 0.70$, indicating that 70% of the variation in D_{50} was explained by the three variables. The mean RMSE was 27 μm (see Table II), which was regarded as acceptable with a mean D_{50} for the 96 subsamples of 66 μm.

This model, termed the VNIR_W model, was statistically significant for the prediction of D_{50} because the significance value (p) of 0.00 was less than the alpha value of 0.05 and the model showed a good overall fit to the data, $F(3, 96) = 71.31$ at $p < 0.05$. The negative β values of all three variables indicated that D_{50} increased with decreasing WC ($t = -6.66$; $p = 0.00$), $R(B8)/R(B3)$ ($t = -9.91$; $p = 0.00$) and $R(B4)$ ($t = -7.17$; $p = 0.00$), where t is the coefficient divided by the standard error in the t–statistic (see Table III). $R(B8)/R(B3)$ was specified as the strongest factor for D_{50} from the magnitudes of β and t. The VNIR_W model is expressed as

$$D_{50} = 487.49 - 763.78 * R(B4)$$

$$- 163.24 * R(B8)/R(B3) - 2.45 * WC. \qquad (2)$$

TABLE III
COEFFICIENTS OF THE VNIR_W MODEL IN TABLE I

	Unstandardized Coefficients		Standardized Coefficients	t	p
	B	Standard error	β		
(Constant)	487.49	29.01		16.80	0.00
R(B8)/R(B3)	-163.24	16.47	-0.59	-9.91	0.00
SWC	-2.45	0.37	-0.51	-6.66	0.00
R(B4)	-763.77	106.49	-0.54	-7.17	0.00

B and β are the standardized regression coefficients and t is a coefficient of the t-statistic.

Fig. 11. Cross-validation of the two regression models. (a) model (1) used for estimating WC and (b) model (2) used for D_{50}, by comparing estimated WC and D_{50} values with those of the subsequent 20 samples. Regression (dotted) and 45 ° lines (broken lines) are overlaid on the scatter plots to indicate overestimations above the 45 ° line and underestimations beneath it.
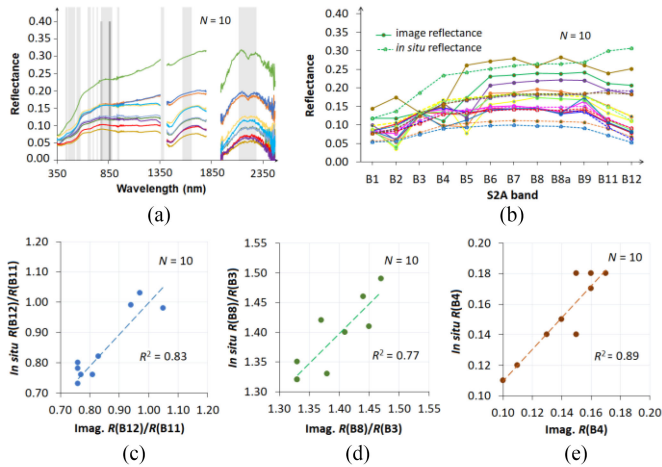

Fig. 10. Consistency of reflectance between field reflectance and S2A image reflectance retrieved through the ELM atmospheric correction method (BOA reflectance). (a) Field reflectance measured at 10 sampling sites on December 17, 2017, (b) Comparisons between simulated S2A band reflectance (*in situ*) and BOA reflectance of the S2A image (imag.); and, scatter-plots of the simulated reflectance and BOA reflectance for (c) B12/B11, (d) B8/B3, and (e) B4 reflectance. The 1:1 line and regression lines are overlaid on the scatter plots.

D. Verification of Regression Models

The reflectance spectra measured at the 10 sites used for the atmospheric correction and the comparisons between simulated S2A band reflectance (*in situ*) and BOA reflectance (image) are shown in Fig. 10(a) and (b), respectively. To confirm the applicability of the S2A image data through the ELM atmospheric correction method, the consistency of the reflectance and band ratios of the *in-situ* data used for WC and D_{50}, R(B4), R(B12)/R(B11), and R(B8)/R(B3) were checked against those of the BOA reflectance in the ten corresponding S2A image pixels on December 17, 2017 using scatter plots [see Fig. 10(c)–(e)]. Because adequate correlations were shown for all three parameters, with an $R^2 \geq 0.75$, the two corrected S2A images were used to estimate WC and D_{50} using models (1) and (2).

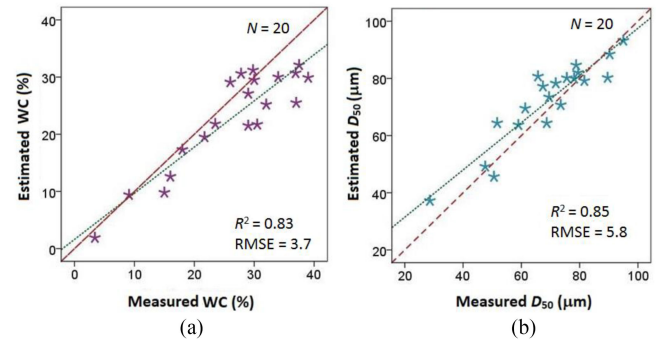The subsequent 20 samples collected on March 12, 2019 were used to verify the accuracy of the regression models for calculating WC and D_{50}. The results are shown in scatter plots between the estimated and measured WC and D_{50} values in Fig. 11(a) and (b), respectively. Fig. 11 supports the reliability of the models with a relatively high R^2 (0.83 and 0.85) and small RMSE (3.7% and 5.8 μm), respectively. A smoothing effect appeared on the WC and D_{50} estimations, i.e., an underestimation of high WC and an overestimation of small D_{50} (see Fig. 11). Therefore, model (1) is not suitable for estimating the WC of silts under saturated conditions and model (2) is not accurate for areas covered by clay and very fine silt. However, clayey areas are often covered by mangroves and very fine silt areas tend to be small on intertidal flats, as reported by [32]. Considering those situations, the proposed regression models are reasonably effective for estimating the WC and D_{50} of intertidal flat sediments.

E. Mapping of WC and Sediment Type Using S2A Image Data

The ranges of estimated WC and D_{50} from the two S2A images were 2%–42.5% and 3.9–140 μm, respectively. Using the estimated D_{50}, sediments were reclassified into six types: very fine silt (D_{50}: 3.9–7.8 μm), fine silt (D_{50}: 7.8–15.6 μm), medium silt (D_{50}: 15.6–31 μm), coarse silt (D_{50}: 31–63 μm), very fine sand (D_{50}: 63–125 μm), and fine sand (D_{50}: 125–250 μm) following the Wentworth scale. The resulting distributions of WC and sediment types are shown in Fig. 12. Because the intertidal flat was narrower in the 2017 image than the 2019 image, the spatial variations of WC and the sediment types are unclear in the 2017 image [see Fig. 12(a) and (b)]. In contrast, a trend of increasing WC from the shoreline toward the land with decreasing D_{50}, i.e., changing from coarse to fine sediments is conspicuous in the 2019 image which shows the entire tidal flat [see Fig. 12(c) and (d)]. Accordingly, this article clarifies that the finer sediments tended to contain higher WC. Low WC zones <10% were mostly the sand bars along the shoreline and zones approximately 2 m higher than MWL [64].

The sediment distribution was characterized by fine sands, coarse silt, and very fine sands which constituted the sand bars, the lowlands close to mangroves, and flat zones between them, respectively. In contrast to these major types, the distribution of
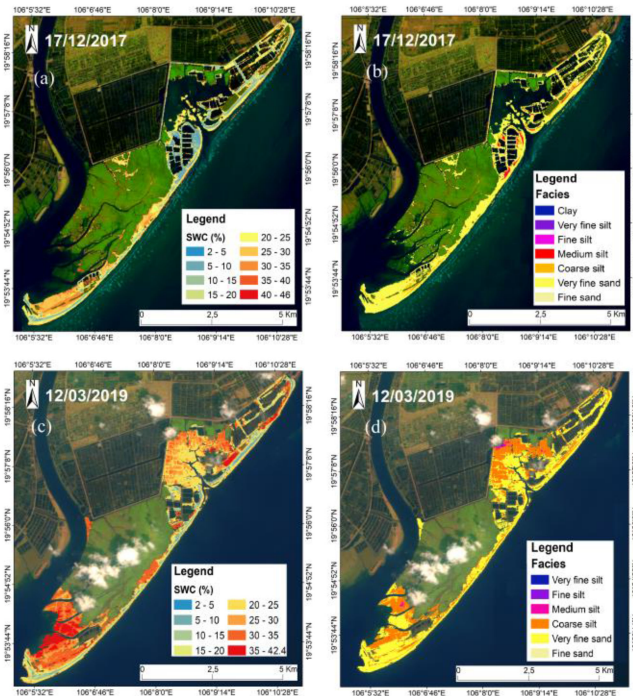
Fig. 12. Distributions of estimated WC and sediment type classified by the D_{50} of surface sediments over the study area using the S2A image data acquired on (a) and (b) December 17,2017 and (c) and (d) March 12, 2019 calculated from (1) and (2). All maps are overlaid on the false-color image as in Fig. 1(b) and (c).

very fine sediments composed of medium silt, fine silt, and very fine silt was limited to small parts of the lowland flats surrounded by coarse silts. The patterns in the article are consistent with the survey results of the Hai Phong Oceanography Institute in 2003 [32], and the map based on *in situ* measurements created by [64]. These consistencies support the accuracy and effectiveness of the proposed regression models and suggest their potential for mapping sediment types over tidal flats along the Red river delta and where other tidal flats occur with similar geographic conditions to the study area.

IV. Discussion

A. Use of SWIR Band Ratio for WC

A variety of models using reflectance data from optical sensor imagery have been proposed for estimating WC based on the absorption and refraction of water at the water–mineral interfaces of electromagnetic waves, including in disciplines, such as soil engineering, agriculture, and environmental applications [65]–[67]. This article revealed that the ratio of reflectance between B11 and B12 was the best for estimating WC using S2A image data. This was demonstrated by a strong negative correlation ($\rho < -0.8$) between the WC of 96 subsamples from dry to saturated conditions and the simulated band ratio [see Fig. 5(c) and (d)]. The selection of B11 and B12 was verified by [68] who revealed the strong dependence of reflectance on WC in these bands, as shown here in Fig. 6(a). It was also verified by [69] who specified that the SWIR band around 2210 nm (B12 in

the article) was the most suitable single band for estimating WC, because its reflectance was the most highly correlated with WC. We found this was common to all the sediment types [see Figs. 5 and 6]. However, the use of single band reflectance for WC estimation is often not adaptable, because the reflectance can change substantially with the condition of electromagnetic waves and the viewing angle of the sample as reported from laboratory-based results [70], as well as with the atmospheric and topographic effects of satellite imagery. Band ratios can reduce these effects by enhancing the reflectance difference between individual bands [71]. Consequently, the present study selected the band ratio model for estimating the WC.

A band ratio approach using an SWIR band around 2200 nm and an NIR band has been applied for soil moisture estimation and drought monitoring in a tropical region [72]. The band ratio, B12/B8, is equivalent to the SWIR/NIR ratio. However, its correlation with WC ($\rho = -0.75$ for all 96 subsamples and $\rho = -0.82$ for the 84 wet sub-samples where WC $> 0\%$), was weaker than the use of B12/B11, where $\rho = -0.81$ and $\rho = -0.86$, for the equivalent samples. The SWIR/NIR ratio is also more suitable for areas with vegetation [68], rather than for the intertidal flats examined in this article. Because NIR reflectance is strongly affected by the leaf dry matter content, rather than by WC, the SWIR/NIR ratio is effective at removing the effect of leaf dry matter content and thus increasing the estimation accuracy of WC in vegetated areas [73]. These reasons led us to avoid the use of NIR reflectance for WC in this article.

B. Use of Regression Models for Sediment GS

An inverse and conspicuous relationship between particle size and $R(\lambda)$, particularly in the SWIR region in the dry state, has been reported by many studies [19], [70], [74], [75]. This relationship can be interpreted as an increase in particle size with increasing surface roughness caused by a rise in self-shadowing effects and multiple scattering and therefore, a decrease in the total surface reflectance in a defined view angle [76]. However, this physics does not always fit with fine sediments as demonstrated in previous studies [77], [78] and also in the results presented here for fine sediments composed of very fine sand, silts, and clay in Figs. 7(a) and 8(a). This inconsistency may be caused by the small variation in the D_{50} of the samples, which led to small differences in the SWIR $R(\lambda)$. Another cause was the change in the colors of samples along with D_{50}, e.g., the very fine silt samples ($D_{50} = 5$–$7~\mu m$) were reddish brown, which indicated the occurrence and deposition of Fe oxides and, accordingly, decreased the overall $R(\lambda)$. In contrast, the fine sand samples ($D_{50} = 163~\mu m$), mainly composed of quartz, were light grey and had relatively large $R(\lambda)$. The dependence of the spectra of dry samples on the color of sediments in addition to the GS, as shown in Figs. 7(a) and 8(a), is also reported by [79]. Therefore, consideration of the red band (B4) reflectance in (2) is appropriate.

By classifying the data into WC classes (0%, 15$\pm$2%, and 20$\pm$2%), strong negative correlations ($\rho < -0.8$) between D_{50} and the NIR band reflectance in B8 and B8a within 785–899 nm range were revealed by this article. This finding agrees with that

of [13] who compared the D_{50} of dry sediments sampled from the tidal flats of the Red river mouth (near our study area) with the NIR band reflectance of ALOS imagery at B4 (760–890 nm) and found a negative correlation between the reflectance and the particle size of dry samples. The interpretation was that there was an increase in the absorption of photons in coarse sediments according to Beer's law [80], [81], because the internal paths of photons in sediment pores become greater with increasing GS. This article demonstrated that the difference in $R(\lambda)$ between the NIR and visible bands was significantly related to D_{50}, which is similar to previous findings [15], [82]. Therefore, the NIR to visible band ratio, B8/B3, was selected for D_{50} estimation, similar to a band ratio of $R(750)/R(420)$ reported by [82] and a band ratio between Landsat TM B2 (visible green: 520–650 nm) and B5 (SWIR: 1550–1750 nm) reported by [15].

Furthermore, this article confirmed a strong effect of WC on the overall reflectance spectrum as shown in Fig. 6, indicating that the overall $R(\lambda)$ decreased substantially with just an increase of 3% in WC from the dry condition. This finding concurs with previous studies [19], [83]. In fact, incorporation of the WC into D_{50} estimation through model (2) improved the estimation accuracy, as shown in Table I.

The selection of the NIR and the VIS band ratio, red band reflectance, and WC as exploratory variables in the regression model for D_{50} estimation is supported by previous findings and, therefore, forms an appropriate method. The accuracy of the regression model was verified in Fig. 11(b), and its effectiveness was demonstrated by the characteristic and valid sediment type distributions through the model [see Fig. 12]. To make the regression model more versatile, coarse sediments, such as medium and coarse sands, which were not distributed in the study area, should be analyzed. In addition, both calibration and validation with field data are indispensable in applying the regression model to other tidal flats.

V. CONCLUSION

To improve remotely-sensed regional monitoring of tideland environments, this article aimed to clarify the effects of WC and GS distribution on the reflectance spectra of surface sediments by focusing on the intertidal flat on the Red river delta coast in Vietnam using S2A image data. Through the analyses of 32 surface sediment samples from the tidal flat, collected on two field visits (12 and 20 samples, respectively), and the measurement of their reflectance spectra, significant correlations were found between the WC and the S2A band ratio, B12/B11 ($\rho = -0.81$), and also between the D_{50} and the band ratio, B8/B3 ($\rho = -0.73$). The overall magnitude of the reflectance spectra changed substantially with the WC, but varied only slightly with D_{50}, which indicates that WC can be estimated directly from B12/B11 while WC also needs to be considered for D_{50} estimation.

The regression models were formulated using data from the initial 12 samples to estimate WC and D_{50}. The best fitted models were a linear function of B12/B11 for WC ($R^2 = 0.93$, RMSE $= 3.19\%$) and a linear multivariate model using an NIR and VIS band ratio (B8/B3), red band (B4) reflectance which could

discriminate the color of sediments, and WC for D_{50} (adjusted $R^2 = 0.70$, RMSE $= 27 \mu m$). The effectiveness of the two regression models was verified by large R^2 and small RMSE for the estimated WC and D_{50} values in the measured subsequent 20 samples ($R^2 = 0.83$; RMSE $= 3.7\%$ and $R^2 = 0.85$; RMSE $= 5.8 \mu m$, respectively).

Using two S2A scenes, the regression models were applied to map the WC and sediment type distributions over the study area by classifying six sediment types (very fine silt, fine silt, medium silt, coarse silt, very fine sand, and fine sand) based on the estimated D_{50} using the Wentworth scale. The features of sediment-type distribution agreed well with the previous field survey results in the study area in that the tidal flat was dominated by fine sediments and the fine sand, silt, and very fine sand were distributed mainly on the sand bars along the coastline, close to the mangroves, and between the silt and fine sand, respectively.

Consequently, our results demonstrate the potential of S2A reflectance data for estimating the physical properties and types of sediment on intertidal flats. The proposed regression models can be applied to monitor the tidal flats along the Red river delta coast and in other tidal flats with similar geographic conditions to this study area.

REFERENCES

[1] F. Montserrat, C. Van Colen, S. Degraer, T. Ysebaert, and P. M. J. Herman, "Benthic community-mediated sediment dynamics," *Mar. Ecol. Prog. Ser.*, vol. 372, pp. 43–59, Dec. 2008.

[2] T. Ysebaert, P. Meire, P. M. J. Herman, and H. Verbeek, "Macrobenthic species response surfaces along estuarine gradients: Prediction by logistic regression," *Mar. Ecol. Prog. Ser.*, vol. 225, pp. 79–95, Jan. 2002, doi: 10.3354/meps225079.

[3] P. L. Hir, W. Roberts, O. Cazaillet, M. Christie, P. Bassou, and C. Bacher, "Characterization of intertidal flat hydrodynamics," *Cont. Shelf Res.*, vol. 20, no. 12/13, pp. 1079–1097, Sep. 2000.

[4] B. J. Koo, K. K. Kwon, and J. H. Hyun, "Effect of environmental conditions on variation in the sediment-water interface created by complex macrofaunal burrows on a tidal flat," *J. Sea Res.*, vol. 58, no. 4, pp. 302–312, Nov. 2007.

[5] Z. Shi and J. Y. Chen, "Morphodynamics and sediment dynamics on intertidal mudflats in China (1961–1994)," *Continental Shelf Res.*, vol. 16, no. 15, pp. 1909–1926, Feb. 1996.

[6] H. Zhao, X. Li, X. Wang, and D. Tian, "Grain size distribution of road-deposited sediment and its contribution to heavy metal pollution in urban runoff in Beijing, China," *J. Hazardous Mater.*, vol. 183, nos. 1–3, pp. 203–210, Nov. 2010.

[7] S. Duquesne, L. C. Newton, L. Giusti, S. B. Marriott, H. J. Stärk, and D. J. Bird, "Evidence for declining levels of heavy-metals in the Severn Estuary and Bristol Channel, U.K. and their spatial distribution in sediments," *Environ. Pollut.*, vol. 143, no. 2, pp. 187–196, Sep. 2006.

[8] D. Martincic, Z. Kwokal, and M. Branica, "Distribution of zinc, lead, cadmium and copper between different size fractions of sediments II. The Krka River Estuary and the Kornati Islands (Central Adriatic Sea)," *Sci. Total Environ.*, vol. 95, pp. 217–225, Jun. 1990.

[9] E. P. Nobi, E. Dilipan, T. Thangaradjou, K. Sivakumar, and L. Kannan, "Geochemical and geo-statistical assessment of heavy metal concentration in the sediments of different coastal ecosystems of Andaman Islands, India," *Estuarine Coastal Shelf Sci.*, vol. 87, no. 2, pp. 253–264, Jan. 2010.

[10] M. P. Rainey, A. N. Tyler, R. G. Bryant, D. J. Gilvear, and P. McDonald, "The influence of surface and interstitial moisture on the spectral characteristics of intertidal sediments: Implications for airborne image acquisition and processing," *Int. J. Remote Sens.*, vol. 21, no. 16, pp. 3025–3038, 2000.

[11] J. Bartholdy and S. Folving, "Sediment classification and surface type mapping in the Danish Wadden Sea by remote sensing," *Netherlands J. Sea Res.*, vol. 20, no. 4, pp. 337–345, Dec. 1986.

[12] J. K. Choi, J. H. Ryu, and J. Eom, "Integration of spatial variables derived from remotely sensed data for the mapping of the tidal surface sediment distribution," *J. Coastal Res.*, vol. SI64, Jan. 2011, pp. 1653–1657.

[13] N. T. Ngoc, N. T. Tue, and K. Koike, "Correlating mass physical properties with ALOS reflectance spectra for intertidal sediments from the Ba Lat Estuary (Northern Vietnam): An exploratory laboratory study," *Geo-Mar. Lett.*, vol. 33, no. 4, pp. 273–284, Apr. 2013.

[14] J. H. Ryu, Y. H. Na, J. S. Won, and R. Doerffer, "A critical grain size for landsat ETM+ investigations into intertidal sediments: A case study of the gomso tidal flats," *Estuarine Coastal Shelf Sci.*, vol. 60, no. 3, pp. 491–502, Jul. 2004.

[15] D. Van Der Wal and P. M. J. Herman, "Regression-based synergy of optical, shortwave infrared and microwave remote sensing for monitoring the grain-size of intertidal sediments," *Remote Sens. Environ.*, vol. 111, no. 1, pp. 89–106, 2007.

[16] G. M. Smith, A. G. Thomson, I. Möller, and J. C. Kromkamp, "Using hyperspectral imaging for the assessment of mudflat surface stability," *J. Coastal Res.*, vol. 20, no. 4, pp. 1165–1175, Sep. 2004.

[17] K. J. Kim, B. J. Kim, B. Y. K. Lee, and J. H. Ryu, " Generation of a large-scale surface sediment classification map using unmanned aerial vehicle (UAV) data: A case study at the Hwang-Do tidal flat, Korea," *Remote Sens.*, vol. 11, no. 3, pp. 229–243, Jan. 2019.

[18] M. G. Yates, A. R. Jones, S. McGrorty, and J. D. Goss-Custard, "The use of satellite imagery to determine the distribution of intertidal surface sediments of the Wash, England," *Estuarine Coastal Shelf Sci.*, vol. 36, no. 4, pp. 333–344, Apr. 1993.

[19] C. Verpoorter, V. Carrère, and J. P. Combe, "Visible, near-infrared spectrometry for simultaneous assessment of geophysical sediment properties (water and grain size) using the spectral derivative–modified Gaussian model," *J. Geophys. Res., Earth Surf.*, vol. 119, no. 10, pp. 2098–2122, Sep. 2014.

[20] J. T. Bushong, R. J. Norman, and N. A. Slaton, "Near-infrared reflectance spectroscopy as a method for determining organic carbon concentrations in soil," *Commun. Soil Sci. Plant Anal.*, vol. 46, no. 14, pp. 1791–1801, 2015.

[21] G. R. Hunt, "Spectral signatures of particulate minerals in the visible and near infrared," *Geophysics*, vol. 42, no. 3, pp. 501–513, Apr. 1975.

[22] G. Okin and T. Painter, "Effect of grain size on remotely sensed spectral reflectance of sandy desert surfaces," *Remote Sens. Environ.*, vol. 89, no. 3, pp. 272–280, 2004.

[23] K. Bottcher, C. Glaber, and S. Mooney, "Examining the relationship between soil structure and soil reflectance using soil pore structure characteristics obtained from image analysis," *Remote Sens. Lett.*, vol. 3, no. 7, pp. 557–565, 2011.

[24] Y. Lv and Z. Sun, "Multi-angular spectral reflectance to characterize the particle size of surfaces of desert and cultivated soil," *Eur. J. Soil Sci.*, vol. 67, no. 3, pp. 253–265, 2016.

[25] Y. Kim, D. H. Jang, N. W. Park, and H. Y. Yoo, "Assessment of landform changes in Baramarae tidal flat, Korea using combined analysis of multi-temporal remote sensing images and grain size measurement data," *J. Mar. Sci. Technol.*, vol. 24, no. 6, pp. 1070–1080, 2016.

[26] S. Fal, M. Maanan, L. Baidder, and H. Rhinane, "The contribution of sentinel-2 satellite images for geological mapping in the south of Tafilalet basin (Eastern Anti-Atlas, Morocco)," *Int. Arch. Photogramm. Remote Sens. Spat. Inf. Sci.*, vol. XLII-4/W12, pp. 75–82, Feb. 2019.

[27] W. Ge, Q. Cheng, L. Jing, F. Wang, M. Zhao, and H. Ding, "Assessment of the capability of sentinel-2 imagery for iron-bearing mineral mapping: A case study in the Cuprite Area, Nevada," *Remote Sens.*, vol. 12, no. 18, pp. 3028–3043, 2020.

[28] H. Van der Werff and F. Van der Meer, "Sentinel-2A MSI and landsat 8 OLI provide data continuity for geological remote sensing," *Remote Sens.*, vol. 8, no. 11, pp. 883–898, 2016.

[29] J. Lin, R. Wang, B. Zhao, and S. Cheng, "A comprehensive scheme for lithological mapping using Sentinel-2A and ASTER GDEM in weathered and vegetated coastal zone, Southern China," *Open Geosci.*, vol. 11, nos. 3-4, pp. 982–996, Dec. 2019.

[30] G. Marchetti, S. Bizzi, B. Belletti, P. Carbonneau, and A. Castelletti, "Orbital grain size mapping from sentinel 2 images," in *Proc. 20th EGU Gen. Assem.*, 2018, vol. 20, pp. 13642–13645.

[31] Center for Oceanography, *Tide Table*, vol. 2017, Hanoi, Vietnam: Sci. Publ. House, 2019.

[32] N. H. Cu *et al.*, "Geologic structure and evolution of tidal flats along Nghia Hung district coastline (Cấu trúc và tiến hóa địa chất vùng bãi triều ven biển Nghĩa Hưng)," *Mar. Resour. Environ.*, vol. 10, pp. 89–105, 2003.

[33] P. D. Clift *et al.*, "Evolving East Asian river systems reconstructed by trace element and Pb and Nd isotope variations in modern and ancient Red River-Song Hong sediment," *Geochem. Geophys. Geosyst.*, vol. 9, no. 4, pp. 1–29, Apr. 2008.

[34] D. P. Roy, J. Li, H. K. Zhang, L. Yan, H. Huang, and Z. Li, "Examination of Sentinel-2A multi-spectral instrument (MSI) reflectance anisotropy and the suitability of a general method to normalize MSI reflectance to nadir BRDF adjusted reflectance," *Remote Sens. Environ.*, vol. 199, pp. 25–38, 2017.

[35] FieldSpec 3 User Manual, ASD Document 600540, ASD Inc. Boulder, CO, USA, 2010.

[36] J. A. Brasi, K. Lee, G. Kvaran, B. L. Markham, and J. A. Pedelty, "The spectral response of the Landsat-8 operational land imager," *Remote Sens*, vol. 6, no. 10, pp. 10232–10251, Oct. 2014,.

[37] G. K. Das, "Sediment grain size," in *Encyclopedia of Estuaries, Encyclopedia of Earth Sciences Series*, M. J. Kennish, Ed., Dordrecht, The Netherlands: Springer, 2016.

[38] R. L. Folk, *The Petrology of Sedimentary Rocks*. Austin, TX, USA: Hemphill Publ., 1974.

[39] C. K. Wentworth, "A scale of grade and class terms for clastic sediments," *J. Geol.*, vol. 30, no. 5, pp. 377–392, 1922.

[40] Standard Test Methods for Particle-Size Distribution (Gradation) of Soils Using Sieve Analysis, D6913M-17, ASTM Int., West Conshohocken, PA, USA, 2017. [Online]. Available: https://www.astm.org

[41] Standard Test Method for Particle-Size Distribution (gradation) of Fine-Grained Soils Using the Sedimentation (Hydrometer) Analysis, D7928-21e1, ASTM Int. West Conshohocken., 2021. [Online]. Available: https://www.astm.org

[42] S. J. Blott and K. Pye, "GRADISTAT: A grain-size distribution and statistics package for the analysis of unconsolidated sediments," *Earth Surf. Processes Landforms.*, vol. 26, no. 11, pp. 1237–1248, Sep. 2001.

[43] Standard Test Methods for Determining the Water (Moisture) Content, ash Content, and Organic Material of Peat and Other Organic Soils, ASTM Int., West Conshohocken, PA, USA, 2020. [Online]. Available: https://www.astm.org

[44] D. H. Mook and C. M. Hoskin, "Organic determinations by ignition: Caution advised," *Estuarine Coastal Shelf Sci.*, vol. 15, pp. 697–699, 1982.

[45] E. B. Dor, C. Ong, and I. C. Lau, "Reflectance measurements of soils in the laboratory: Standards and protocols," *Geoderma*, vol. 245, pp. 112–124, 2015.

[46] W. P. Kustas and J. M. Norman, "Use of remote sensing for evapotranspiration monitoring over land surfaces," *Hydrol. Sci. J.*, vol. 41, no. 4, pp. 495–516, 1996.

[47] G. M. Smith and E. J. Milton, "The use of the empirical line method to calibrate remotely sensed data to reflectance," *Int. J. Remote Sens.*, vol. 20, no. 13, pp. 2653–2662, 1999.

[48] N. T. T. Ha, N. T. P. Thao, K. Koike, and M. T. Nhuan, "Selecting the best band ratio to estimate chlorophyll-a concentration in a tropical freshwater lake using sentinel 2A images from a case study of Lake Ba Be (Northern Vietnam)," *ISPRS Int. J. Geo-Inf.*, vol. 6, no. 9, pp. 290–304, Sep. 2017.

[49] A. Ariza, M. Robredo Irizar, and S. Bayer, "Empirical line model for the atmospheric correction of Sentinel-2A MSI images in the Caribbean Islands," *Eur. J. Remote Sens.*, vol. 51, no. 1, pp. 765–776, Jan. 2018.

[50] M. Xu *et al.*, "A spectral space partition guided ensemble method for retrieving chlorophyll-a concentration in inland waters from Sentinel-2A satellite imagery," *J. Great Lakes Res.*, vol. 45, no. 3, pp. 454–465, 2019.

[51] E. V. Shein, E. Y. Milanovskii, and A. Z. Molov, "The effect of organic matter on the difference between particle-size distribution data obtained by the sedimentometric and laser diffraction methods," *Eurasian Soil Sci.*, vol. 39, no. 1, pp. 84–90, Dec. 2006.

[52] S. L. Goodbred and Y. Saito, "Tide-dominated deltas," in *Principles of Tidal Sedimentology*, R. A. Davis and R. W. Dalrymple, Eds., Dordrecht, The Netherlands: Springer, 2012, pp. 129–149.

[53] P. G. E. F. Augustinus, "Actual development of the Chenier coast of Suriname (South America)," *Sedimentary Geol.*, vol. 26, no. 1-3, pp. 91–113, Apr. 1980.

[54] X. Wang and X. Ke, "Grain-size characteristics of the extant tidal flat sediments along the Jiangsu Coast, China," *Sedimentary Geol.*, vol. 112, no. 1/2, pp. 105–122, 1997.

[55] S. Tanabe, Y. Saito, Q. L. Vu, T. J. J. Hanebuth, Q. L. Ngo, and A. Kitamura, "Holocene evolution of the Song Hong (Red River) delta system, Northern Vietnam," *Sedimentary Geol.*, vol. 187, no. 1/2, pp. 29–61, May 2006.

[56] V. T. T. Hoai and N. V. Huyen, "Material and sedimentation characteristics of the Kim Son alluvial ground (Ninh Binh)," *Vietnam J. Earth Sci.*, vol. 31, no. 2, pp. 148–157, Jun. 2009.

[57] B. W. Flemming, "Tidal flats," in *Encyclopedia of Sediments and Sedimentary Rocks. Encyclopedia of Earth Sciences Series*, Dordrecht, The Netherlands: Springer, 1978, pp. 734–737.

[58] S. Vanino *et al.*, "Capability of sentinel-2 data for estimating maximum evapotranspiration and irrigation requirements for tomato crop in Central Italy," *Remote Sens. Environ.*, vol. 215, pp. 452–470, Sep. 2018.

[59] E. Ben-Dor, J. R. Irons, and G. F. Epema, "Soil reflectance," in *Remote Sensing for the Earth Sciences: Manual of Remote Sensing 3/3*, A. N. Rencz, Ed., New York, NY, USA: Wiley, 1999, pp. 111–188.

[60] R. D. Jarrard and M. V. Berg, "Sediment mineralogy based on visible and near-infrared reflectance spectroscopy," *Geological Soc.*, vol. 267, no. 1, pp. 129–140, Jan. 2006.

[61] D. Heller Pearlshtien and E. Ben-Dor, "Effect of organic matter content on the spectral signature of iron oxides across the VIS–NIR spectral region in artificial mixtures: An example from a red soil from Israel," *Remote Sens.*, vol. 12, no. 12, pp. 1960–1974, 2020.

[62] T. Cudahy *et al.*, "Satellite-derived mineral mapping and monitoring of weathering, deposition and erosion," *Sci. Rep.*, vol. 6, pp. 23702–23713, 2016.

[63] L. Zhao *et al.*, "Assessing the utility of visible-to-shortwave infrared reflectance spectroscopy for analysis of soil weathering intensity and paleoclimate reconstruction," *Palaeogeography Palaeoclimatol. Palaeoecol.*, vol. 512, pp. 80–94, Dec. 2018.

[64] V. T. T. Hoai and N. V. Huyen, "Characteristics of sediments on tidal flats from Ba Lat Estuary to Day Estuary," *Vietnam J. Mar. Sci. Technol.*, vol. 10, no. 3, pp. 53–67, Dec. 2012.

[65] R. A. Viscarra Rossel and A. B. McBratney, "Laboratory evaluation of a proximal sensing technique for simultaneous measurement of soil clay and water content," *Geoderma*, vol. 85, no. 1, pp. 19–39, Jul. 1998.

[66] D. B. Lobell and G. P. Asner, "Moisture effects on soil reflectance," *Soil Sci. Soc. Amer. J.*, vol. 66, no. 3, pp. 722–727, May 2002.

[67] A. Kaleita, L. F. Tian, and M. C. Hirschi, "Relationship between soil moisture content and soil surface reflectance," *Trans. ASAE*, vol. 48, no. 5, pp. 1979–1986, 2005.

[68] J. Yue, J. Tian, Q. Tian, K. Xu, and N. Xu, "Development of soil moisture indices from differences in water absorption between shortwave-infrared bands," *ISPRS J. Photogramm. Remote Sens.*, vol. 154, no. 8, pp. 216–230, Jul. 2019.

[69] M. Sadeghi, S. B. Jones, and M. Tuller, "Toward a calibration-free model for optical remote sensing of soil moisture," in *Proc. AGU Fall Meeting*, 2015.

[70] Z. Sun, Y. Lv, and Z. Tong, "Effects of particle size on bidirectional reflectance factor measurements from particulate surfaces," *Opt Exp.*, vol. 24, no. 6, pp. 612–634, Mar. 2016.

[71] T. M. Lillesand, R. W. Kiefer, and J. W. Chipman, *Remote Sensing and Image Interpretation*, New York, NY, USA: Wiley, 1999.

[72] N. T. Dinh, N. T. T. Ha, T. D. Quy, K. Koike, and M. T. Nhuan, "Effective band ratio of landsat 8 images based on VNIR-SWIR reflectance spectra of topsoils for soil moisture mapping in a tropical region," *Remote Sens.*, vol. 11, no. 6, pp. 716–733, Feb. 2019.

[73] P. Ceccato, S. Flasse, S. Tarantola, S. Jacquemoud, and J. M. Grégoir, "Detecting vegetation leaf water content using reflectance in the optical domain," *Remote Sens. Environ.*, vol. 77, no. 1, pp. 22–33, Jul. 2001.

[74] T. L. Myers *et al.*, "Quantitative reflectance spectra of solid powders as a function of particle size," *Appl. Opt.*, vol. 54, no. 15, pp. 4863–4875, May 2015.

[75] M. Sadeghi, E. Babaeian, M. Tuller, and S. B. Jones, "Particle size effects on soil reflectance explained by an analytical radiative transfer model," *Remote Sens. Environ.*, vol. 210, pp. 375–386, Jun. 2018.

[76] M. F. Baumgardner, L. F. Silva, L. L. Biehl, and E. R. Stoner, "Reflectance properties of Soils," *Adv. Agronomy*, vol. 38, pp. 1–44, 1986.

[77] E. M. M. Novo, J. D. Hansom, and P. J. Curran, "The effect off sediment type on the relationship between reflectance and suspended sediment concentration," *Int. J. Remote Sens.*, vol. 10, no. 7, pp. 1283–1289, 1989.

[78] B. J. Kim, S. Lee, and H. Lee, "Spectral reflectance of mongsanpo tidal flat, Korea, by using spectroradiometer experiments and landsat data," *Korean J. Remote Sens.*, vol. 33, no. 4, pp. 411–422.

[79] M. P. C. Lacerda, J. A. M. Demattê, M. V. Sato, C. T. Fongaro, B. C. Gallo, and A. B. Souza, "Tropical texture determination by proximal sensing using a regional spectral library and its relationship with soil classification," *Remote Sens.*, vol. 8, no. 9, pp. 701–720, Aug. 2016.

[80] M. F. Baumgardner, L. F. Silva, L. L. Biehl, and E. R. Stoner, "Reflectance properties of soils," *Adv. Agronomy*, vol. 38, pp. 1–44, 1986.

[81] R. N. Clark, "Spectroscopy of rocks and minerals, and principles of spectroscopy," in *Manual of Remote Sensing (vol. 3), Remote Sensing For the Earth Sciences*, A. N. Rencz, Ed. New York, NY, USA: Wiley, 1999, pp. 3–58.

[82] H. Hakvoort, K. Heymann, C. Stein, and D. Murphy, "In-situ optical measurements of sediment type and phytobenthos of tidal flats: A basis for imaging remote sensing spectroscopy," *German J. Hydrogr.*, vol. 49, no. 2/3, pp. 367–373, Sep. 1997.

[83] C. Small *et al.*, "Spectroscopy of sediments in the Ganges-Brahmaputra delta: Spectral effects of moisture, grain size and lithology," *Remote Sens. Environ.*, vol. 113, no. 2, pp. 342–361, Feb. 2009.

Vu Thi Thu Thuy received the B.Sc. and M.Sc. degrees in geology from Vietnam National University, Hanoi, Vietnam, in 2010 and 2012, respectively. She is currently working toward the Ph.D. degree in environmental geosphere engineering with the Graduate School of Engineering, Kyoto University, Kyoto, Japan.

She is currently a Junior Lecturer with Falculty of Geography, Hanoi National University of Education, Hanoi, China. Her research interests include assessing the environmental and natural resources in coastal zone, and application of remote sensing for monitoring coastal line and sediments.

Nguyen Thi Thu Ha received the B.Sc. and M.Sc. degrees in geology from Vietnam National University, Hanoi, Vietnam, in 2000 and 2004, respectively and the Ph.D. degree in environmental and earth sciences from Kumamoto University, Kumamoto, Japan, in 2011.

She is currently an Associate Professor with the University of Science, Vietnam National University, Hanoi, Vietnam. Her research interest include monitoring water quality in coastal and inland waters using remote sensing date, hyperspectral remote sensing of earth materials, and modeling vulnerability, and resilience to geo-disasters.

Katsuaki Koike received the B.Sc., M.Sc., and Ph.D. degrees in earth resources engineering from Kyoto University, Kyoto, Japan, in 1986, 1988, and 1995, respectively.

In 1988, he was a Research Assistant on engineering geology with Kumamoto University, where he was a Professor in the field of Hydro- and Geosphere Environmental Sciences in 2005. Since April 2011, he has been a Professor with the Laboratory of Environmental Geosphere Engineering, Kyoto University. His research themes include various disciplines of the Earth Science and Technology, but can be summarized into three categories: remote sensing for clarifying Earth environments and geosphere structures, applied geophysics and geochemistry for integrated imaging of geologic structures, and mathematical modeling for geosphere environments using geostatistics and geoinformatics. Spatial and genetic clarification of mineral, geothermal, and groundwater resources through these methods especially is his interest.

Nguyen Thien Phuong Thao received the B.Sc. and M.Sc. degrees in natural resources and environmental management from Vietnam National University, Hanoi, Vietnam, in 2016 and 2020, respectively.

She is currently a Junior Researcher with the Faculty of Geology, University of Science, Vietnam National University, Hanoi, Vietnam. Her research interests include application of remote sensing for monitoring lake and river water quality, floods, and drought mapping.

Dinh Xuan Thanh received the B.Sc., M.Sc., and Ph.D. degrees in geology from the University of Science, Vietnam National University, Hanoi, Vietnam, in 1997, 2002, and 2012, respectively.

He is currently an Associate Professor with the University of Science, Vietnam National University, Hanoi, Vietnam. His research interests include sedimentology, marine geology, and geologic mapping.

Pham Ngoc Trung received the B.Sc. degree in geology in 2020 from the University of Science, Vietnam National University, Hanoi, Vietnam, where he is currently working toward the master's degree in geology.

He is currently a Junior Researcher with the Sea and Island Research Center of Faculty of Geology, University of Science, Vietnam National University, Hanoi, Vietnam. His research interests involve application of remote sensing for geology and geodisaster mapping.